



Massively parallel finite element simulation of compressible and incompressible flows

T.E. Tezduyar*, S.K. Aliabadi, M. Behr, S. Mittal

AEM/AHPCRC, Supercomputer Institute, University of Minnesota, 1200 Washington Avenue South, Minneapolis, MN 55415, USA

Received 4 February 1994

Revised manuscript received 10 February 1994

Abstract

We present a review of where our research group stands in parallel finite element simulation of flow problems on the Connection Machines, an effort that started for our group in the fourth quarter of 1991. This review includes an overview of our work on computation of flow problems involving moving boundaries and interfaces, such as free surfaces, two-liquid interfaces, and fluid-structure and fluid-particle interactions. With numerous examples, we demonstrate that, with these new computational capabilities, today we are at a point where we routinely solve practical flow problems, including those in 3D and those involving moving boundaries and interfaces. We solve these problems with unstructured grids and implicit methods, with some of the problem sizes exceeding 5 000 000 equations, and with computational speeds up to two orders of magnitude higher than what was previously available to us on the traditional vector supercomputers.

1. Introduction

In this review article, we report on where we are now, roughly two years after we first started, in the fourth quarter of 1991, implementing our finite element formulations of flow problems on the connection Machine family of supercomputers from Thinking Machines Corporation. We also report on where we are nearly three and half years after we started, in the third quarter of 1990, our computations of flow problems involving moving boundaries and interfaces. This article contains material extracted from articles by these authors and their coworkers, which appeared recently or are about to appear.

In mid-1990, with the deformable-spatial-domain/stabilized-space-time (DSD/SST) formulation (Tezduyar et al. [1, 2]), we initiated the development of what turned out to be a powerful, general-purpose numerical capability for solving a large class of compressible and incompressible flow problems involving moving boundaries and interfaces, such as free surfaces, two-liquid interfaces, and fluid-structure and fluid-particle interactions. Changes in the shape of the spatial domain with respect to time are taken into account automatically by the DSD/SST formulation, because this formulation is written over the space-time domain of a problem.

The stabilization is achieved by employing, typically, for compressible flows the streamline-upwind/Petrov-Galerkin (SUPG) formulation [3–5], and for incompressible flows the Galerkin/least-squares (GLS) formulation [6, 7]. For compressible flows, we use conservation variables formulations of the Euler and Navier-Stokes equations. The SUPG stabilization technique for compressible flows was introduced in [3]. In recent years this technique was enhanced by a shock-capturing term [4, 5], and this

* Corresponding author.

enhancement rendered this technique very comparable in accuracy to those that followed [3] and formulated in entropy variables [8, 9]. The stabilized space–time formulation was used in the past by other researchers to solve flow problems with fixed spatial domains [7, 9, 10]. For incompressible flows, when the spatial domain is fixed, i.e. when the problem does not involve any moving boundaries or interfaces, then, to avoid the cost associated with the space–time formulation, we prefer to use the pressure-stabilizing/Petrov–Galerkin (PSPG) formulation [11, 12], which can be cast in the context of a semi-discrete formulation. With these stabilization techniques, we can handle flows at high Mach and Reynolds numbers, as well as flows with shocks and sharp boundary layers, with minimal numerical dissipation. Furthermore, the stabilized nature of these formulations allows us to use equal-order interpolation functions for velocity and pressure.

In flow problems involving moving boundaries and interfaces, to update the mesh as the spatial domain deforms with time, special mesh moving techniques as well as automatic mesh moving methods are used to minimize, and in some cases totally eliminate, the need for remeshing (i.e. the need for generating a new set of nodes and elements). Remeshing involves projection errors, and in 3D problems, the cost of repetitive mesh generation and parallelization set up (following each remeshing) could be prohibitive. For these reasons, we find mesh update strategies which minimize the frequency of remeshing desirable. With special mesh moving schemes designed for specific problems and geometries, we were able to solve, with no need for remeshing, a number of problems, such as air intake of a jet engine with adjustable spool [13–15], vortex-induced vibrations of a cylinder [16–19], flow past a pitching airfoil [17–19], dynamics of an airfoil falling in a fluid [18, 20, 21], and flow-induced vibrations of a flexible pipe [21, 22].

In a more general setting, for problems with more complicated or significantly varying geometries, we use a general-purpose, automatic mesh moving scheme [18, 23–25] in which the nodal motions are governed by the equations of elasticity, with the boundary conditions determined by the motion of the free surfaces, interfaces and solid boundaries. Similar mesh moving schemes were used earlier by other researchers [26]. In our approach, we drop from the finite element formulation the Jacobian of the transformation between the physical and finite element domains, and this results in keeping the shape of the smaller elements more intact compared to the larger elements. With this approach, we have solved several problems, such as dynamics of a liquid drop falling in a fluid [18, 23–25], flow past an oscillating airfoil [23–25], and flow past two airfoils with one of them oscillating [25]. In these problems involving airfoils, we use structured meshes with quadrilateral elements near the airfoils, and unstructured meshes with triangular elements elsewhere. The structured meshes undergo rigid-body motion with the airfoils, while the unstructured meshes are moved with the automatic mesh moving schemes described above. Even with this automatic mesh moving scheme, sometimes it becomes necessary to remesh; but the idea is to minimize the frequency of remeshing, as we did in solving the problem of flow through a sluice gate [25]. Detailed description of these mesh update schemes and several examples can be found in [25].

We started implementing our incompressible flow formulations on the Connection Machines in the fourth quarter of 1991. We reported our first results in [18], and we were soon able to solve a large class of practical flow problems, such as simple fluid–body and fluid–structure interactions [18–21], including those in 3D [21, 22], and several 3D problems [21–24, 27–29], including those involving free surfaces [23, 24, 27]. In all these computations the parallel implementation is based on the assumption that the mesh is unstructured, and this gives us a parallel performance with little dependence on the complexity of the geometry and mesh. Furthermore, all these computations are based on implicit time-integration methods.

Our massively parallel computations of compressible flows started in early 1992, with our first results reported in [23]. A later version of [23] appeared as a journal article [24]. The compressible flow problems we consider come mostly from aerospace applications. These computations include those in 3D, such as flows past projectiles [23, 24], simple models of aerospace vehicles [14, 15, 23, 24], and commercial aircraft [14, 15]. These computations also include those involving moving boundaries and interfaces, such as air intake of jet engine with adjustable spool [14, 15]. In compressible flow computations, for time-integration we typically use implicit methods, although we also have the capability to use, and have in fact used, explicit methods in some problems.

These new computational capabilities are now allowing us to solve problems which we were not able to attempt before. Today, essentially all our computations are carried out on the massively parallel platforms of the Connection Machines, mainly on a CM-5 with 512 processing nodes with computational speeds which are two orders of magnitude higher than what was available to us two to three years ago on the traditional vector supercomputers. Today we routinely solve time-dependent, 3D flow problems, even 3D problems with moving boundaries and interfaces. Among the time-dependent, 3D incompressible flow problems solved are, flow between two concentric cylinders for a range of Reynolds numbers (with 282 000 + Eqs.), sloshing in a container subjected to vertical vibrations (52 000 + Eqs.), flow past a sphere (388 000 + Eqs.), flow around a submarine (466 000 + Eqs.), flow past a rectangular wing (320 000 + Eqs.), and flow-induced vibrations of a flexible pipe (145 000 + Eqs.). Among the steady-state, 3D compressible flow problems solved are, subsonic flow past a sphere (720 000 + Eqs.), supersonic flow past a missile (1 100 000 + Eqs.), supersonic flow past a delta-wing (5 000 000 + Eqs.), and inviscid, transonic flow past an aircraft (513 000 + Eqs.). The delta-wing and submarine problems were featured, respectively, on the cover pages of the Slide Book of the ARPA High Performance Computing Software PI Meetings in Norfolk, Virginia, 17–18 March 1993 and in San Diego, California, 27–29 September 1993.

2. Governing equations

In this section, we state the problem in the form of first incompressible, and then compressible, Navier–Stokes equations. In the following, $\Omega_t \subset R^{n_{sd}}$ will denote a bounded region at time $t \in (0, T)$, with boundary Γ_t , where n_{sd} is the number of space dimensions. The time index indicates that the domain may be deforming. The symbols $\rho(x, t)$, $u(x, t)$, $p(x, t)$ and $e(x, t)$ will represent the density, velocity, pressure and the total (internal plus kinetic) energy fields, respectively. The external forces, such as the gravity, will be represented by $f(x, t)$.

2.1. Incompressible flows

The Navier–Stokes equations for incompressible flows are

$$\rho \left(\frac{\partial u}{\partial t} + u \cdot \nabla u - f \right) - \nabla \cdot \sigma = 0 \quad \text{on } \Omega_t, \quad \forall t \in (0, T), \quad (1)$$

$$\nabla \cdot u = 0 \quad \text{on } \Omega_t, \quad \forall t \in (0, T), \quad (2)$$

where ρ is assumed to be constant. For the Newtonian flows under consideration here, the stress tensor for a fluid with dynamic viscosity μ is defined as follows:

$$\sigma = -pI + 2\mu\epsilon(u). \quad (3)$$

This equation set is completed by suitable boundary conditions and an initial condition consisting of a divergence-free velocity field specified over the entire domain:

$$u(x, 0) = u_0, \quad \nabla \cdot u_0 = 0 \quad \text{on } \Omega_0. \quad (4)$$

2.2. Compressible flows

The Navier–Stokes equations for compressible flows can be written in the vector form

$$\frac{\partial U}{\partial t} + \frac{\partial F_i}{\partial x_i} - \frac{\partial E_i}{\partial x_i} = 0 \quad \text{on } \Omega_t, \quad \forall t \in (0, T), \quad (5)$$

where $U = (\rho, \rho u_1, \rho u_2, \rho u_3, \rho e)$, is the vector of conservation variables, F_i and E_i are, respectively, the Euler and viscous flux vectors defined as

$$F_i = \begin{pmatrix} u_i \rho \\ u_i \rho u_1 + \delta_{i1} p \\ u_i \rho u_2 + \delta_{i2} p \\ u_i \rho u_3 + \delta_{i3} p \\ u_i (\rho e + p) \end{pmatrix}, \tag{6}$$

$$E_i = \begin{pmatrix} 0 \\ \tau_{i1} \\ \tau_{i2} \\ \tau_{i3} \\ -q_i + \tau_{ik} u_k \end{pmatrix}, \tag{7}$$

τ_{ik} are the components of the Newtonian viscous stress tensor, and q_i are the components of the heat flux. Here the equation of state is modeled with the ideal gas equation.

Alternatively, Eq. (5) can be written in the quasi-linear form

$$\frac{\partial U}{\partial t} + A_i \frac{\partial U}{\partial x_i} - \frac{\partial}{\partial x_i} \left(K_{ij} \frac{\partial U}{\partial x_j} \right) = 0 \quad \text{on } \Omega, \quad \forall t \in (0, T), \tag{8}$$

where

$$A_i = \frac{\partial F_i}{\partial U}, \tag{9}$$

$$K_{ij} \frac{\partial U}{\partial x_j} = E_i. \tag{10}$$

It is assumed that appropriate sets of boundary and initial conditions are specified with Eq. (8).

3. Finite element formulations

In a space–time formulation, the space–time domain is first divided into a sequence of space–time slabs Q_n , and each slab is decomposed into space–time elements Q_n^c . A slab Q_n is located between the time levels t_n and t_{n+1} . The integration of a functional over a slab will include integration over both the spatial domain Ω , and the temporal one $[t_n, t_{n+1}]$. Since many of the functions introduced in the following subsection will be discontinuous across slab interfaces, we will employ the notation $(\cdot)_n^-$ and $(\cdot)_n^+$ to indicate the values at t_n as it is approached from below and above, respectively. The number of elements in slab n is written as $(n_{el})_n$.

3.1. Incompressible flows

The finite element formulation begins with choosing appropriate trial solution $((\mathcal{V}_u^h)_n$ and $(\mathcal{V}_p^h)_n$) and weighting function $((\mathcal{V}_u^h)_n$ and $(\mathcal{V}_p^h)_n = (\mathcal{S}_p^h)_n$) spaces for the velocity and pressure. In our computations we employ piecewise linear functions for all fields.

The stabilized space–time formulation for deforming domains can be written as follows: given $(u^h)_n^-$, find $u^h \in (\mathcal{V}_u^h)_n$ and $p^h \in (\mathcal{S}_p^h)_n$ such that $\forall w^h \in (\mathcal{V}_u^h)_n$ and $\forall q^h \in (\mathcal{V}_p^h)_n$

$$\begin{aligned} & \int_{Q_n} w^h \cdot \rho \left(\frac{\partial u^h}{\partial t} + u^h \cdot \nabla u^h - f \right) dQ + \int_{Q_n} \varepsilon(w^h) : \sigma(p^h, u^h) dQ \\ & + \int_{Q_n} q^h \nabla \cdot u^h dQ + \int_{\Omega_n} (w^h)_n^+ \cdot \rho ((u^h)_n^+ - (u^h)_n^-) d\Omega \\ & + \sum_{e=1}^{(n_{el})_n} \int_{Q_n^c} \tau_{MOM} \frac{1}{\rho} \left[\rho \left(\frac{\partial w^h}{\partial t} + u^h \cdot \nabla w^h \right) - \nabla \cdot \sigma(q^h, w^h) \right] \end{aligned}$$

$$\begin{aligned} & \cdot \left[\rho \left(\frac{\partial \mathbf{u}^h}{\partial t} + \mathbf{u}^h \cdot \nabla \mathbf{u}^h - \mathbf{f} \right) - \nabla \cdot \boldsymbol{\sigma}(\rho^h, \mathbf{u}^h) \right] dQ \\ & + \sum_{e=1}^{(n_{el})_n} \int_{Q_n^e} \tau_{\text{CONT}} \nabla \cdot \mathbf{w}^h \rho \nabla \cdot \mathbf{u}^h dQ = \int_{(P_n)_h} \mathbf{w}^h \cdot \mathbf{h}^h dP. \end{aligned} \quad (11)$$

Here \mathbf{h}^h represents the Neumann boundary condition imposed, $(P_n)_h$ is the part of the slab boundary with such conditions, and τ_{MOM} and τ_{CONT} are the stabilization parameters. The solution to (11) is obtained sequentially for all space–time slabs Q_1, Q_2, \dots, Q_{N-1} , and the computations start with

$$(\mathbf{u}^h)_0^- = \mathbf{u}_0^h. \quad (12)$$

The deformation of the mesh is reflected in the deformation of space–time elements, and is automatically accounted for when computing the transport terms. In the formulation given by Eq. (11), the first four integrals, together with the right-hand side, represent the time-discontinuous Galerkin formulation of (1)–(2). The fourth integral weakly enforces the continuity of the velocity field in time. The two series of element-level integrals in the formulation are the least-squares stabilization terms. The reader can refer to [1, 2, 27] for further details regarding the space–time formulation for incompressible flows, including definitions of the stabilization parameters. For problems not involving moving boundaries and interfaces, a semi-discrete formulation derived from Eq. (11) can be written by dropping the fourth integral and the term $\partial \mathbf{w}^h / \partial t$, and by converting all space–time integrations to spatial integrations.

3.2. Compressible flows

In finite element formulation of compressible flows, we define the function spaces \mathcal{S}_n^h and \mathcal{V}_n^h corresponding to the trial solutions and weighting functions, respectively. Again, we use first-order polynomials as interpolation functions. Globally, these functions are continuous in space but discontinuous in time.

The DSD/SST formulation of (8) can be written as follows: given $(U^h)_n^-$, find $U^h \in \mathcal{S}_n^h$ such that $\forall \mathbf{W}^h \in \mathcal{V}_n^h$

$$\begin{aligned} & \int_{Q_n} \mathbf{W}^h \cdot \left(\frac{\partial \mathbf{U}^h}{\partial t} + A_i^h \frac{\partial \mathbf{U}^h}{\partial x_i} \right) dQ + \int_{Q_n} \left(\frac{\partial \mathbf{W}^h}{\partial x_i} \right) \cdot \left(K_{ij}^h \frac{\partial \mathbf{U}^h}{\partial x_j} \right) dQ + \int_{\Omega_n} (\mathbf{W}^h)_n^+ \cdot ((U^h)_n^+ - (U^h)_n^-) d\Omega \\ & + \sum_{e=1}^{(n_{el})_n} \int_{Q_n^e} \boldsymbol{\tau} (A_k^h)^T \left(\frac{\partial \mathbf{W}^h}{\partial x_k} \right) \cdot \left[\frac{\partial \mathbf{U}^h}{\partial t} + A_i^h \frac{\partial \mathbf{U}^h}{\partial x_i} - \frac{\partial}{\partial x_i} \left(K_{ij}^h \frac{\partial \mathbf{U}^h}{\partial x_j} \right) \right] dQ \\ & + \sum_{e=1}^{(n_{el})_n} \int_{Q_n^e} \left(\frac{\partial \mathbf{W}^h}{\partial x_i} \right) \cdot \left(\frac{\partial \mathbf{U}^h}{\partial x_i} \right) dQ = \int_{(P_n)_h} \mathbf{W}^h \cdot \mathbf{H}^h dP. \end{aligned} \quad (13)$$

The solution to (13) is obtained sequentially for Q_1, Q_2, \dots, Q_{N-1} , commencing with

$$(U^h)_0^- = U_0^h, \quad (14)$$

where U_0 is the initial value of the vector U .

In the formulation (13), the first three integrals, together with the right-hand side, represent the time-discontinuous Galerkin formulation of (8). The third integral weakly enforces the continuity of the conservation variables in time. The first series of element-level integrals are the SUPG stabilization terms, and the second series are the shock-capturing terms added to the formulation. The definition of $\boldsymbol{\tau}$ and δ are given in [13]. For problems not involving moving boundaries and interfaces, a semi-discrete formulation derived from Eq. (13) can be written by dropping the third integral, and by converting all space–time integrations to spatial integrations.

4. Parallel implementation

With the advent of parallel computing, a new degree of difficulty has been added to the numerical code development. New algorithms not only have to be efficient from the scalar and vector point of view, but must also exhibit scalable performance when executing in parallel on hundreds or thousands of interconnected processors. In this section, we provide an overview of our data parallel approach to implementing finite element methods on the Connection Machine range of supercomputers. The details of the implementation can be found in [19, 29].

A common starting point for the design of a brand-new parallel implementation of a finite element code on a distributed memory machine like the CM-5 is the decision regarding distribution of the variables among the processing nodes. One of the natural data storage modes is an element-level mode in which one element and all of its associated variables and parameters reside in the local memory of a single processing node. This necessarily leads to duplication of certain quantities, such as nodal coordinates, which would be stored at a node-level in a conventional implementation. However, this kind of data distribution will allow a majority of operations in a finite element program to proceed in parallel without any inter-processor communication whatsoever. The phase of the program which deals with GMRES iterations [30] to solve the linear equation system obtained from the finite element discretization, will require another data structure, either node-level or an equation-level one. Although the differences between these two alternatives are minor, our implementations employ the equation-level structures. Here, all data associated with a single entry of the equation system resides on a single processing node, again rendering many steps of the GMRES iterations communication-free.

The two kinds of data structures will interact mainly in GMRES iterations, and it is here that the communication issues become important. The mapping between the two data sets is determined by the element connectivity and the numbering of global degrees-of-freedom, or equations. Note that this numbering, as well as the numbering of elements, are not unique and can be adjusted to produce the best data locality. Although the preceding approach is applicable to any machine which supports data parallel programming model, such as Cray T3D or MasPar, it highly benefits from the features included in the Connection Machine Scientific Software Library (CMSSL) available on the Connection Machine computers. The communication between the element-level and equation-level data can be performed using the highly optimized CMSSL gather and scatter routines. These routines have the ability to save various communication trace information in order to achieve much faster subsequent gathers and scatters if the communication pattern is unchanged. Equally important are the CMSSL utilities for partitioning the finite element mesh into subdomains, grouping elements belonging to each subdomain on a single processing node, and suitably aligning the equation-level data with the reordered element-level data. The CMSSL communication routines can exploit the resulting data locality, and perform significant portion of the gather and scatter operations referencing only the local memory of the processing nodes.

5. Examples

In this section, we describe our numerical examples in two parts: incompressible and compressible flows. Except for the first problem in each part, all examples presented here are 3D simulations. In all problems we employ a GMRES iterative solver. Except where noted, these problems were computed on the CM-5.

5.1. Incompressible flows

Dynamics of a falling airfoil

In this 2D simulation we study the dynamics of a NACA 0012 airfoil falling in a viscous fluid. Of interest here is the effect of the location of the center of gravity of the airfoil on its pitch stability. The motion of the airfoil is governed by Newton's laws of motion. The mass and the polar moment of inertia of the airfoil are 4.07 and 0.22, respectively. The center of gravity of the airfoil is located on the chord

line, at 0.42 chord-lengths from the leading edge. The finite element mesh consists of 8446 nodes and 8304 quadrilateral elements. At every time step 49 992 non-linear equations are solved to update the flow field. Zero velocity is specified at the inflow boundaries and traction-free conditions are imposed at the outflow boundaries. The entire mesh is moved with the velocity of the mid-chord point of the airfoil.

At $t=0$, the airfoil is released from rest at 10° angle with the line of gravity. Results from this simulation were reported in Mittal and Tezduyar [20]; after a while the airfoil reaches a temporally periodic motion. In addition to having a translatory motion, there is a superimposed pitching motion. The first four frames in Fig. 1 show the vorticity field for this simulation during one period of the pitch motion of the airfoil. The average Reynolds number for this periodic solution (based on the translational velocity of the airfoil and its chord length) is approximately 225.

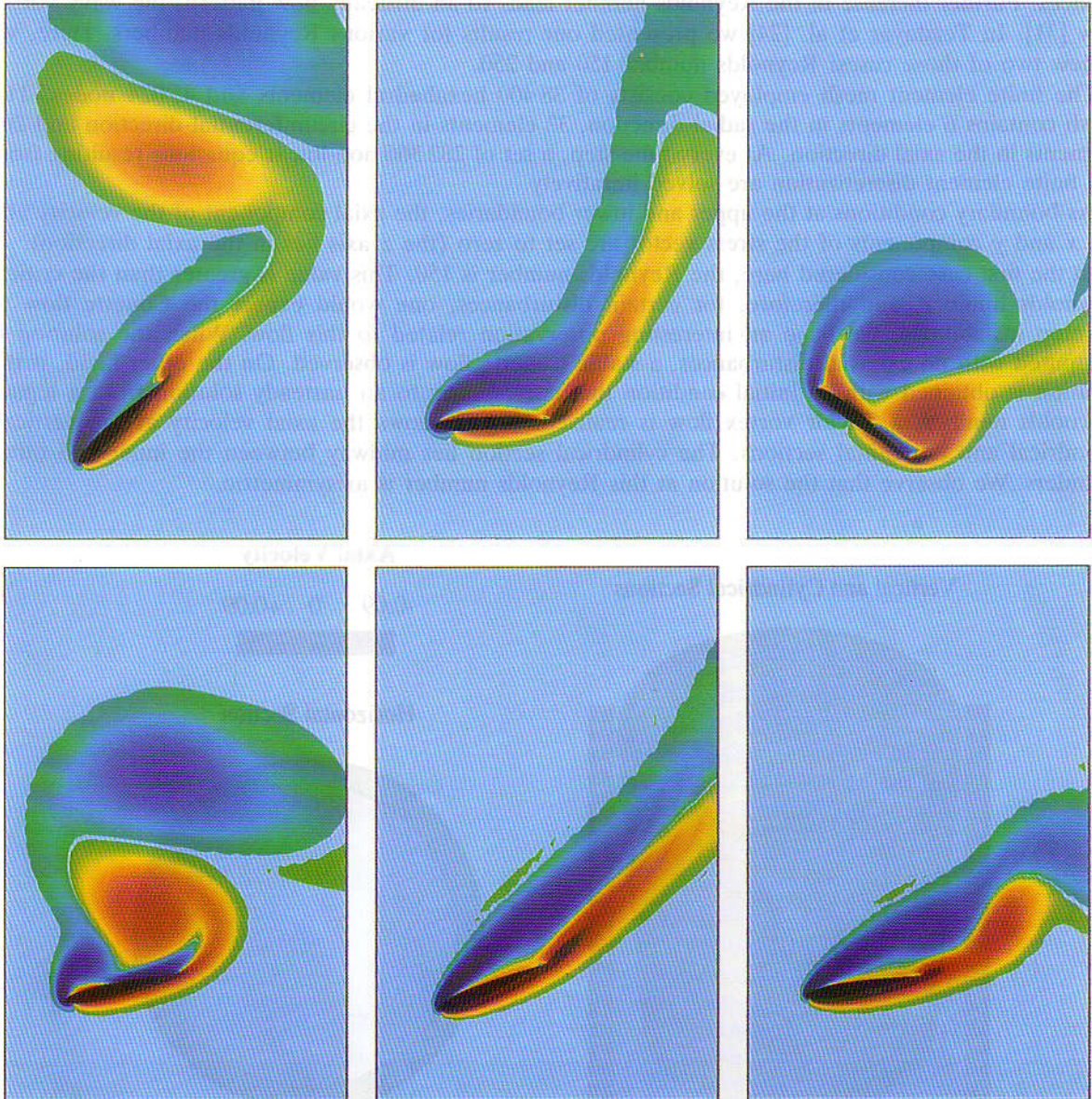


Fig. 1. 2D incompressible flow simulation of the dynamics of an airfoil falling in a viscous fluid. In the first part of the simulation the center of gravity is located at 0.42 chord-lengths from the leading edge: in the second part it is moved to 0.30 chord-lengths. This change results in higher pitch stability for the airfoil. The first four images show the vorticity field for the first part of the simulation, and the last two images for the second part.

In the next part of this simulation, the center of gravity of the airfoil is moved to 0.30 chord-lengths from the leading edge. This change results in a higher pitch stability for the airfoil. The last two frames in Fig. 1 show the vorticity field for this part of the simulation. We observe that in this case, the motion of the airfoil is primarily translational. The glide angle of the airfoil is approximately 80° with the line of gravity; the Reynolds number is approximately 320. More details about this simulation can be found in Mittal and Tezduyar [22]. This simulation was carried out on the CM-5 and CM-200.

Flow between two concentric cylinders (Taylor-Couette flow)

The purpose of this set of computations is to simulate the instabilities that develop between two concentric cylinders in relative rotation. The Reynolds number is based on the gap size between the two cylinders and the speed of the inner cylinder; the outer cylinder is at rest. Beyond a certain critical Reynolds number, the regular Couette flow becomes unstable and one sees the development of Taylor vortices. Further increase in the Reynolds number leads to an unsteady flow pattern, the wavy vortex flow [31]. In Tezduyar et al. [24] we presented our results for various Reynolds numbers. Here, we review two of those cases: Reynolds number 150 and 250.

The finite element mesh employed consists of 38 400 hexahedral elements and 45 024 nodes. The mesh contains 6 elements in the radial direction, 32 elements in the circumferential direction and 200 elements in the axial direction. At every time step, a set of 282 366 non-linear equations resulting from the finite element discretization are solved iteratively.

As boundary conditions at the upper and lower boundaries, the axial component of the velocity and the x and y components of the stress vector are set to zero (the z axis lies in the axial direction).

In the first case considered here, the Reynolds number is 150. This value is greater than the critical Reynolds number, and therefore, for certain disturbances, one would expect the Couette flow to develop instabilities. We have an interesting observation related to this flow. When the solution is computed with no external disturbances, a stable Couette flow is observed. On the other hand, if the solution is obtained with an initial condition that corresponds to an unsteady solution from a higher Reynolds number, a Taylor vortex flow is realized. Fig. 2 shows the axial velocity at the vertical, cylindrical and horizontal sections. The cylindrical section lies midway between the inner and outer cylinders. We observe that the solution at this Reynolds number is axisymmetric.

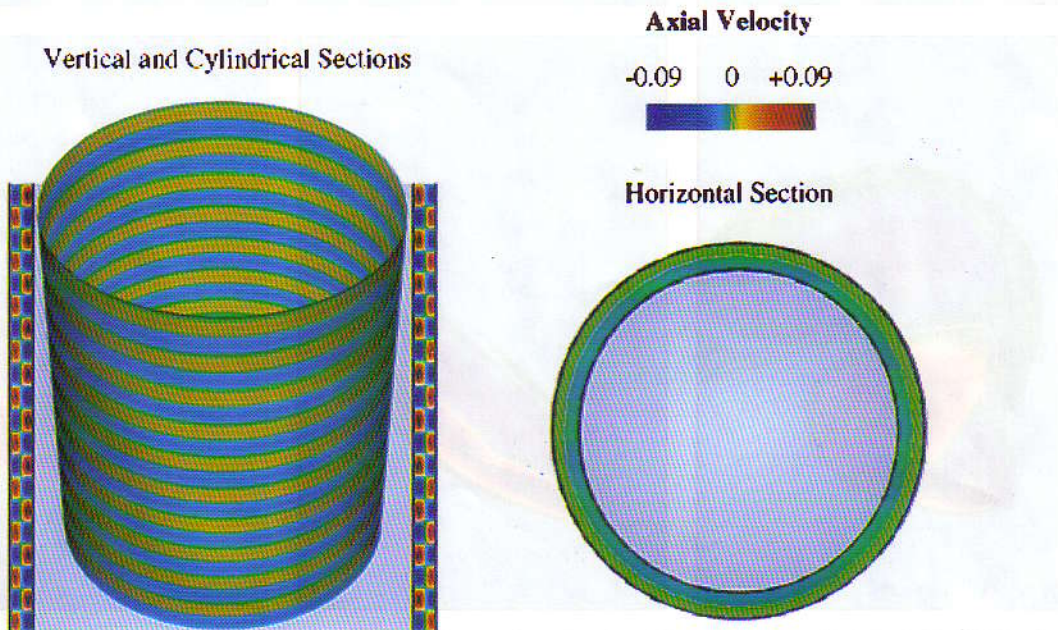


Fig. 2. 3D incompressible flow between two concentric cylinders. The outer cylinder is fixed, and the inner one is spinning at Reynolds number 150. At this Reynolds number the flow is axisymmetric. The images show the axial velocity at vertical, cylindrical and horizontal sections. Number of non-linear equations solved at every time step is 282 000+.

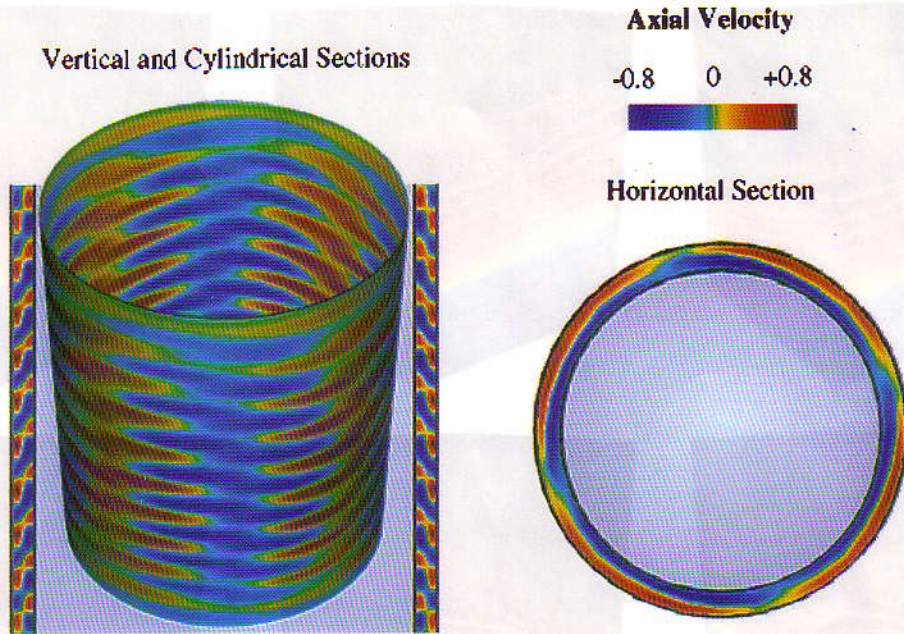


Fig. 3. 3D incompressible flow between two concentric cylinders. The outer cylinder is fixed, and the inner one is spinning at Reynolds number 250. At this Reynolds number the flow is 3D and involves four waves traveling in azimuthal direction. The images show the axial velocity at vertical, cylindrical and horizontal sections. Number of non-linear equations solved at every time step is 282 000+.

At Reynolds number 250, our computations reveal the presence of wavy vortex flow. At this Reynolds number the solution is no longer axisymmetric and involves 3D instabilities. Fig. 3 shows the axial velocity at the vertical, cylindrical and horizontal sections for a nearly temporally periodic solution. We observe that, in addition to the cells in the axial direction, there are four waves traveling in the azimuthal direction.

Sloshing in a container subjected to vertical vibrations

Here we perform a 3D study of sloshing in a container subjected to vertical vibrations. The experimental and theoretical evidence [32] indicates the existence of multiple solution branches when the horizontal cross-section of the container is nearly square. Depending on the frequency of the vibrations, the competing wave modes interact generating complex periodic, as well as chaotic, wave behavior. The particular case considered here is based on the experiment performed by Feng and Sethna [32].

A fuller description of this simulation is given in [27], with only the most significant facts outlined here. The horizontal cross section of the tank is a $W \times H$ rectangle, where $W = 0.178$ m and $H = 0.180$ m. The water level, initially flat, is at $D = 0.127$ m. Side and bottom boundaries allow slip in the direction tangent to the surface. The open surface of the water is assumed to be free from normal and shear stresses, and it moves consistently with the normal component of the fluid velocity at the surface. The external forces acting on the fluid consist of a constant gravitational acceleration of magnitude $g = 9.81 \text{ ms}^{-2}$ and of a sinusoidal vertical excitation $Ag \sin \omega t$ with $\omega = 2\pi f$, $f = 4.00$ Hz and A such that the amplitude of the oscillations remains at 1 mm. The spatial mesh for each time slab consists of 7056 nodes and 6000 quadrilinear brick elements which result in 52 878 equations being solved using the GMRES solver. Fig. 4 shows, at 9 equally-spaced instants during the simulation, the free-surface displacement and the pressure field. This simulation was carried out on the CM-200.

Flow around a submarine

Here we simulate three-dimensional flow around a Los Angeles-class submarine. We use the stabilized space-time method. The Reynolds number based on the free-stream velocity and the hull

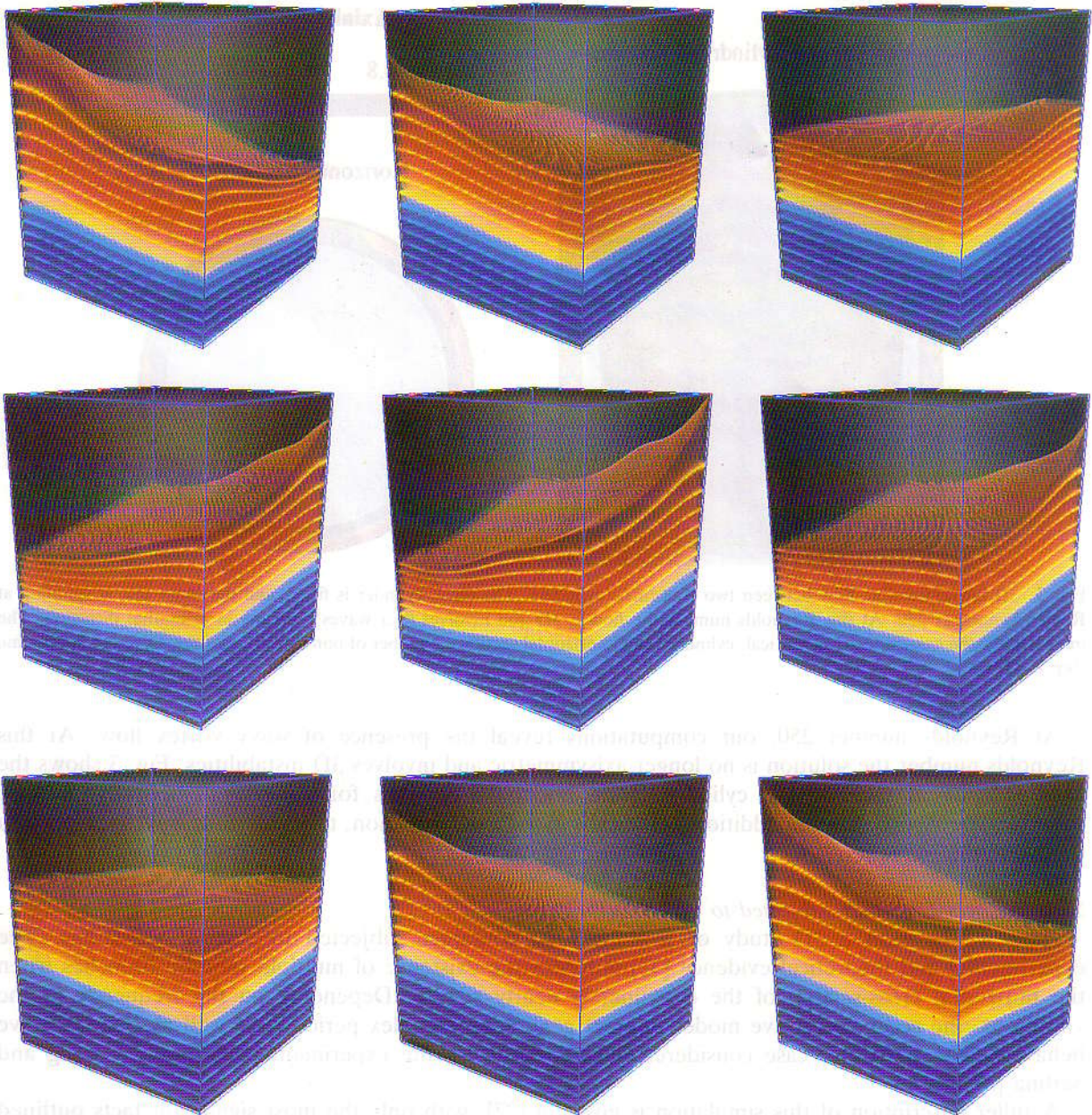


Fig. 4. 3D simulation of sloshing in a container partially filled with water and subjected to vertical vibrations. The images show the free surface and the pressure field. Number of non-linear equations solved at every time step is 52 000+.

length is 1×10^9 . A Smagorinsky turbulence model [33] was used in this unsteady computation, which was restarted from a steady-state solution at Reynolds number 1×10^6 . A similar problem is described in more detail in [29]. We employed a spatial mesh consisting of 71 035 nodes and 345 129 tetrahedral elements. This has resulted in 466 688 equations solved using GMRES iterations. Fig. 5 shows the pressure field on the submarine surface, as well as a set of streamlines at a single instant during the unsteady computation.

With the Krylov space dimension of 40, and 5 outer iterations, a single non-linear iteration took approximately 30 seconds on a CM-5 with 512 processing nodes, and the computations proceeded at an overall rate of 7.0 GigaFLOPS.

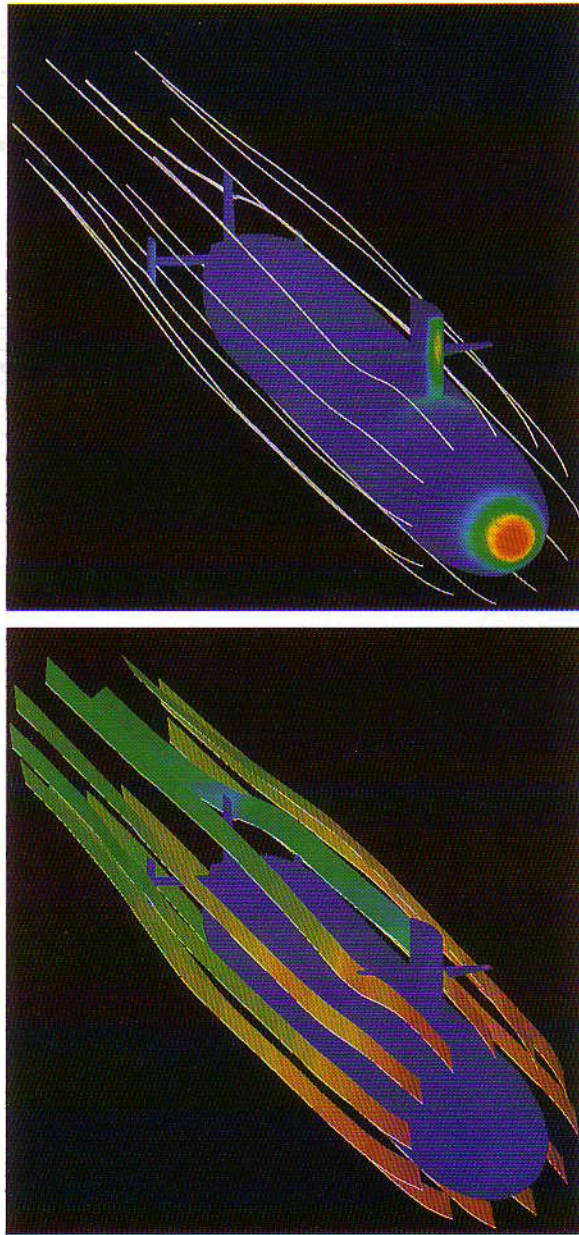


Fig. 5. Flow around a Los Angeles-class submarine. Number of non-linear equations solved at every time step is 466 000+. The top image shows the streamlines and the pressure distribution on the surface of the submarine. The second image shows the stream ribbons color-coded with the axial velocity. These images appeared on the cover page of the Slide Book of the ARPA High Performance Computing Software PI Meeting, San Diego, California, 27-29 September 1993.

3D flow past a rectangular wing

This 3D computation involves flow past a fixed rectangular wing at an angle of attack of 15° . The wing has an aspect ratio of 3 and its cross section is a NACA 0015 airfoil. The Reynolds number, based on the inflow velocity and the chord-length of the wing, is 10 000. The finite element mesh consists of 84 058 nodes and 79 104 hexahedral elements. At every time step 320 563 non-linear equations are solved to update the flow field.

Figure 6 shows the flow field at the wing surface and a cross-section at a certain time instant, from a preliminary computation [21]. The top image shows the pressure distribution on the wing surface and

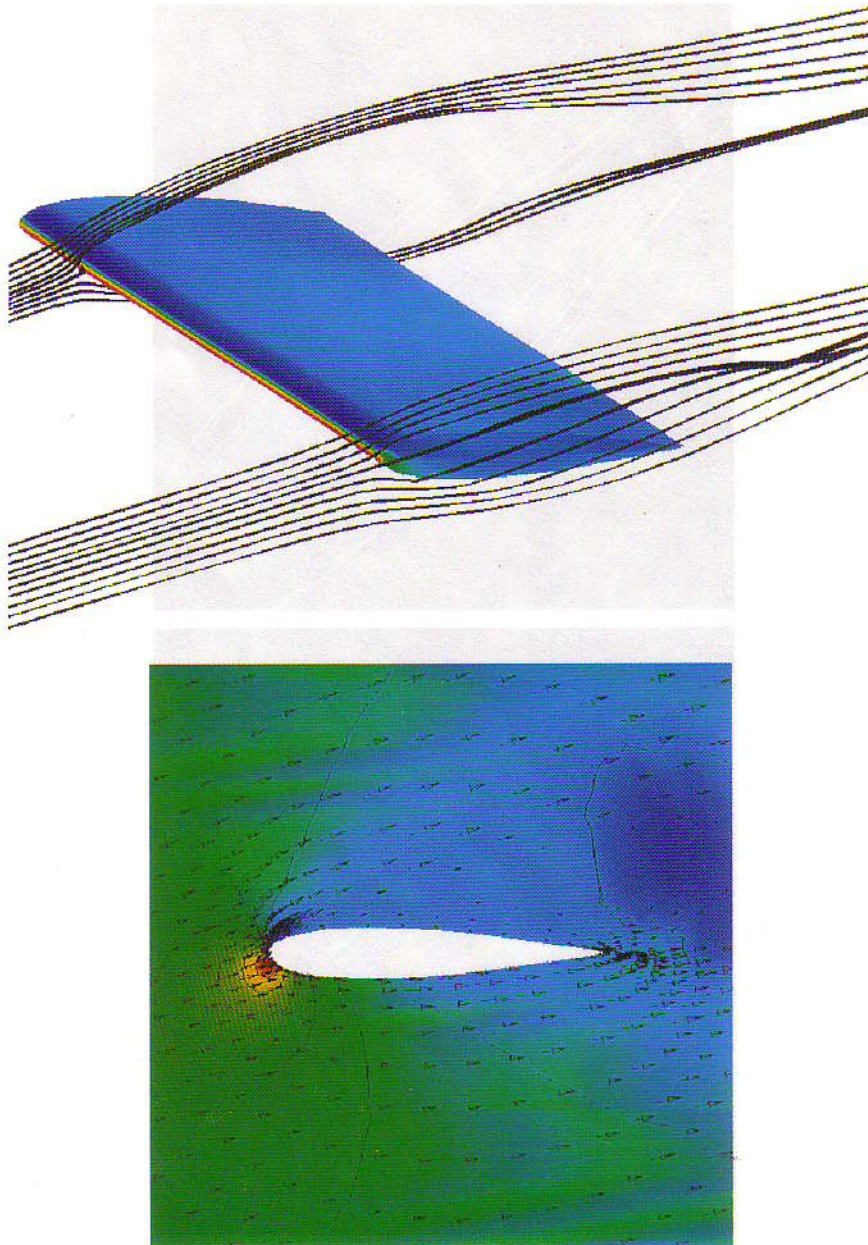


Fig. 6. 3D incompressible flow past a rectangular wing at Reynolds number 10 000. The top image shows the pressure distribution on the wing surface and the streamlines at two different cross-sections. The second image shows the pressure field and the velocity vectors at a cross-section. Number of non-linear equations solved at every time step is 320 000+.

the streamlines at two cross-sections. As expected, these streamlines suggest the presence of wing-tip vortices. The second image shows the pressure field and the velocity vectors at a cross-section. Interested readers are referred to Mittal and Tezduyar [22] for more details.

Flow-induced vibrations of a cantilevered, flexible pipe

In this fluid-structure interaction problem, we simulate the 3D flow in a cantilevered, flexible pipe and the response of the pipe to this flow. The deformation of the pipe, assumed to be planar, is governed by the Bernoulli–Euler beam theory and this limits the reliability of our results to small deformations of the pipe. It is known that beyond a certain critical inflow velocity, the pipe exhibits

flow-induced oscillations [34]. In this simulation the Reynolds number, based on the pipe diameter and the inflow velocity at the pipe centerline, is 1000. The length of the pipe is 20 times its diameter.

The finite element mesh consists of 20 449 nodes and 18 720 hexahedral elements. At every time step 145 298 non-linear equations are solved to update the flow field. The structural part of the problem involves solution of 240 equations at every time step.

Fig. 7 shows the flow field in the pipe section in its plane of motion during a full period of oscillations. The images in the left column show the pressure field, and the ones in the right column show the lateral component of velocity. From these pictures we observe that the pipe exhibits the second mode of cantilevered beam oscillations. More details about these computations can be found in Mittal and Tezduyar [22]. This simulation was carried out on the CM-200.

5.2. Compressible flows

Air intake of a jet engine at Mach 2 and Reynolds number 0.8 million

This axisymmetric computation demonstrates the potential of the DSD/SST formulation to model intricate compressible flows involving interactions between boundary layers, shocks and moving surfaces. This type of flow is encountered in the air intake of a jet engine with adjustable spool. The efficiency of these engines at supersonic speeds can be improved by moving the spool back and forth and thus adapting the outstanding shock. The free-stream Mach number is 2, and the Reynolds number based on the free-stream values and the gap size is 0.8 million. We use 48 450 quadrilateral elements and 49 091 nodes. At each time step, 386 974 non-linear equations are solved simultaneously. Computation starts with the free-stream values as initial condition, and after a prescribed period of time the spool starts to move forward.

The mesh moving strategy used for this problem is such that the connectivity of the mesh remains unchanged throughout the simulation. This eliminates the projection errors associated with remeshing and also eliminates the parallelization overhead associated with remeshing. The images in Fig. 8 show the Mach number at six different instants during the motion of the spool. A full problem description and discussion can be found in [15]. This simulation was carried out on the CM-200.

3D flow past a sphere at Mach 0.1

We solved this 3D problem for a set of Reynolds numbers ranging from 30 to 200 to demonstrate the reliability of our method at low Mach number flows. Here the Reynolds number is based on the free-stream values and the diameter of the sphere. The free-stream Mach number is 0.1. At this low Mach number, the variations in density are less than 0.5%. This allows us to compare our steady-state results with incompressible flow data from Schlichting [35].

The mesh used to solve this problem consists of 148 969 nodes and 142 364 hexahedral elements. For the time integration, an explicit method is used, and 720 657 non-linear equations are solved at each time step. Computed and experimental drag coefficients compare very well. Fig. 9 shows the pressure distribution on the surface of the sphere and in the symmetry plane. See [15] for more details.

3D flow past a delta-wing at Mach 3 and Reynolds number 1.1 million

In this problem, we consider the flow of air past a delta-wing model of an aerospace vehicle at Mach 3. The Reynolds number based on free-stream values and the maximum chord length (along the plane of symmetry) is 1.1 million. Due to the assumed symmetry of the solution, only half of the flow over the delta-wing is computed.

The delta-wing has a wedge type cross section as an underbody in which its corners merge smoothly to the flat surface on the top. The delta-wing has unit length in the chordwise direction and is tapered from 0.0 to 0.69 units in the spanwise direction. The surface geometry of the delta-wing was provided to us by Dr. Chien Li from NASA-JSC. Our preliminary steady-state solution of this problem was obtained on a relatively coarse mesh, with 152 397 nodes and 143 920 hexahedral elements (see [24]). This solution is presented in Fig. 10 with two images showing the side and front views of the delta-wing together with the Mach number distribution around it. Later, we solved this problem with a mesh consisting of 1 032 328 nodes and 1 002 684 hexahedral elements. In this case, 5 001 031 non-linear

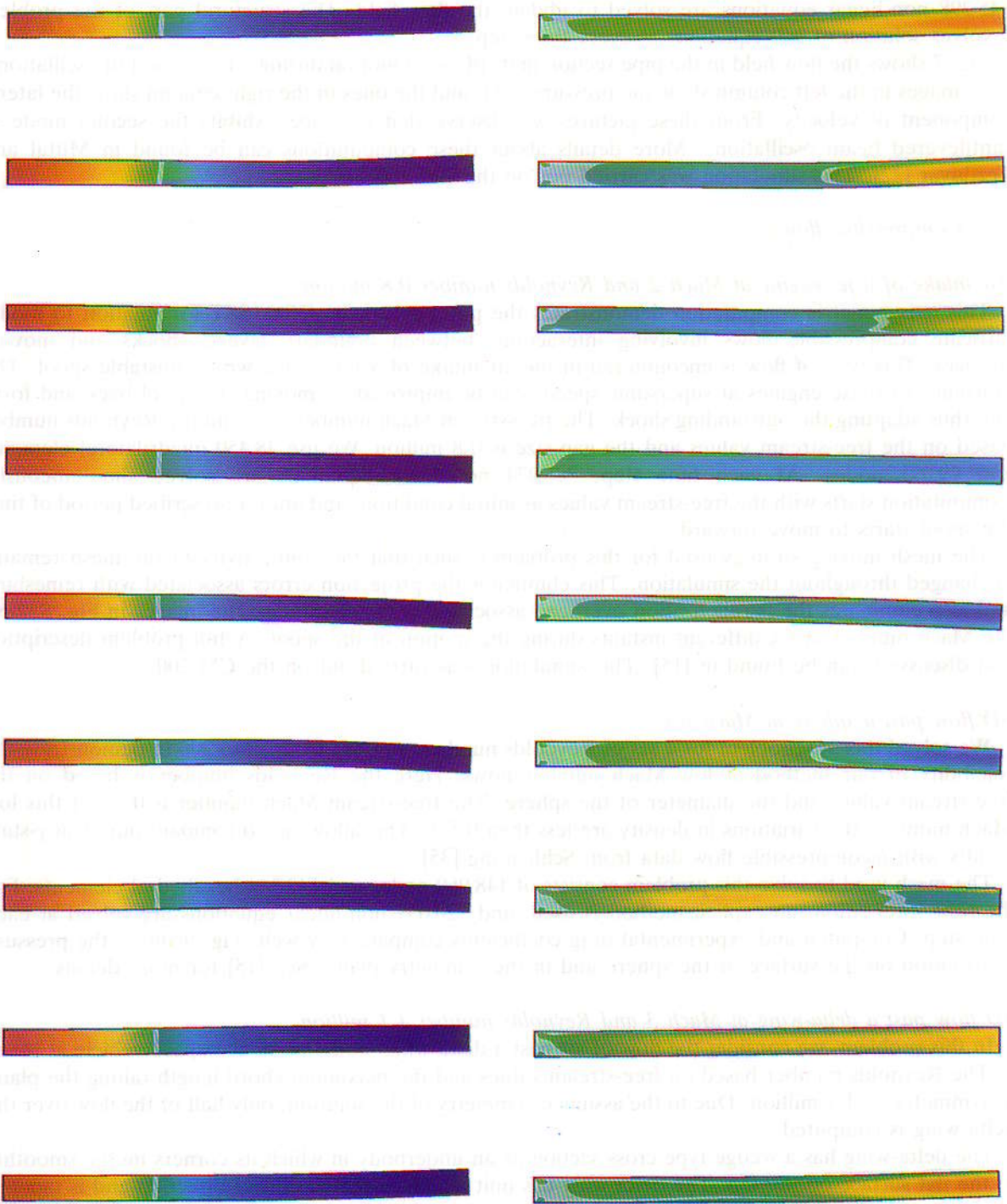


Fig. 7. Flow-induced vibrations of a cantilevered, flexible pipe with 3D incompressible flow at Reynolds number 1000. The images show the pressure (left column) and lateral velocity (right column) in the pipe section in its plane of motion during a full period of oscillations. Number of non-linear equations solved to update the flow field at every time step is 145 000+. The structural part of the problem, governed by a 1D model, involves solution of 240 equations at every time step.

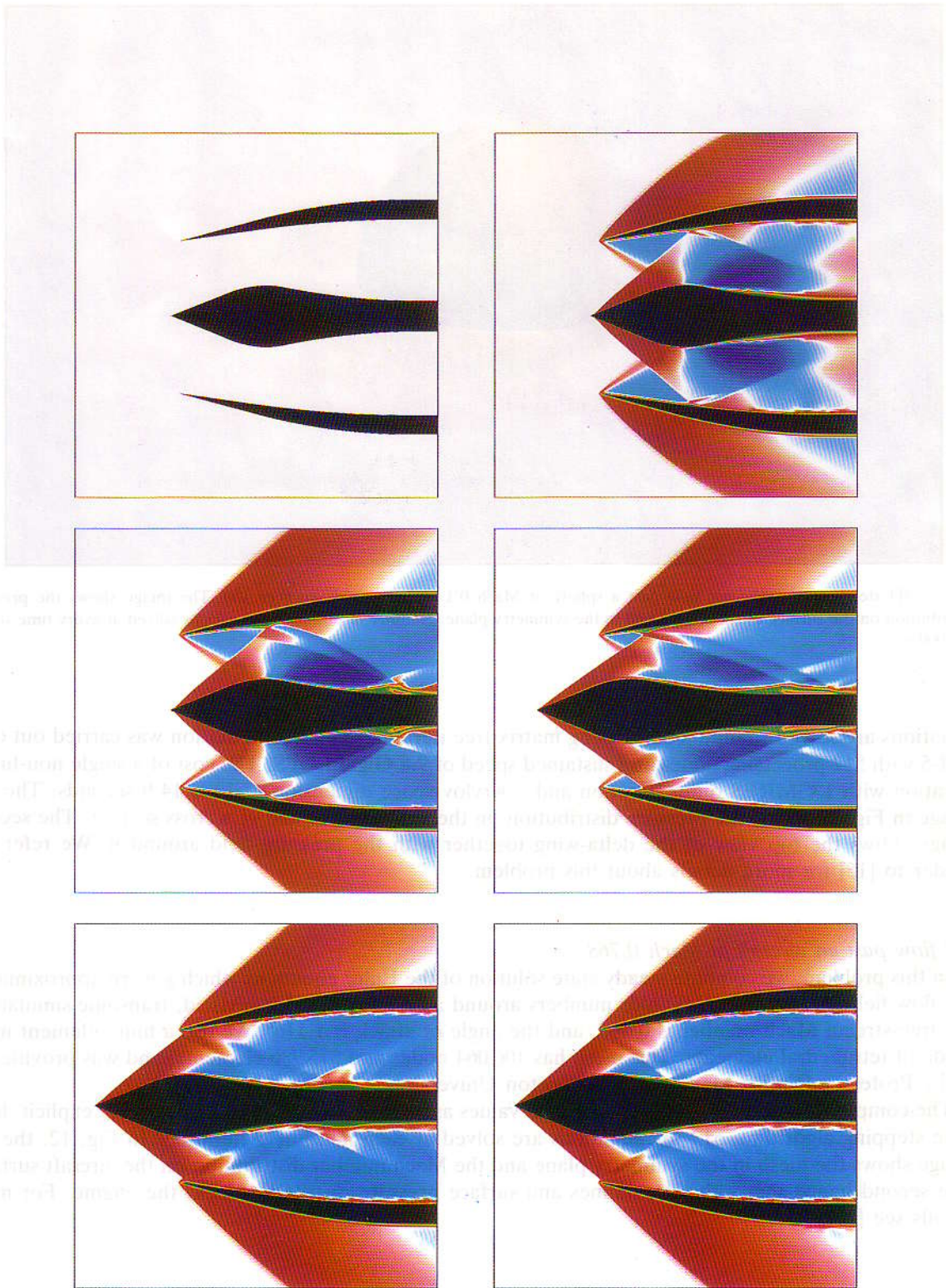


Fig. 8. Axisymmetric simulation of air intake of a jet engine with adjustable spool at Mach 2 and Reynolds number 0.8 million. The images show the Mach number at six different instants during the motion of the spool. Number of non-linear equations solved at every time step is 386 000+.

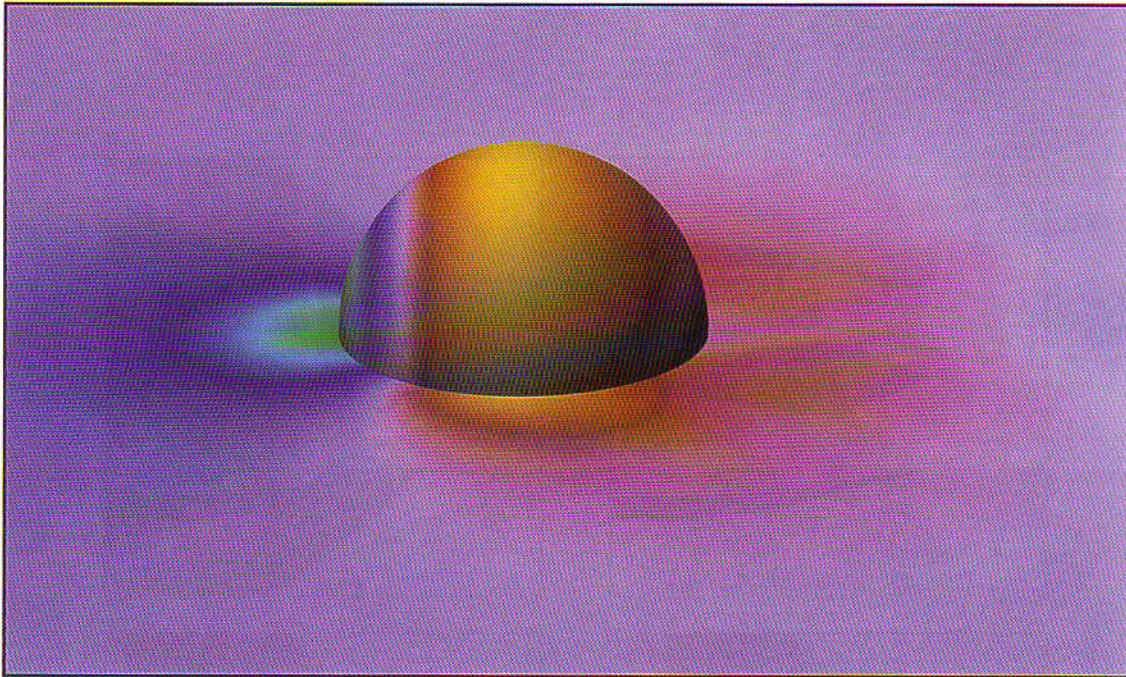


Fig. 9. 3D steady-state, subsonic flow past a sphere at Mach 0.1 and Reynolds number 100. The image shows the pressure distribution on the surface of the sphere and in the symmetry plane. Number of non-linear equations solved at every time step is 720 000+.

equations are solved simultaneously using matrix-free iterations. This computation was carried out on a CM-5 with 512 processing nodes at a sustained speed of 9.8 GigaFLOPS. The cost of a single non-linear iteration with 1 GMRES outer iteration and a Krylov space dimension of 10 is 14.9 seconds. The top image in Fig. 11 shows the pressure distribution on the wing surface and at a cross section. The second image shows the top view of the delta-wing together with the pressure field around it. We refer the reader to [15] for more details about this problem.

3D flow past an aircraft at Mach 0.768

In this problem, we compute steady-state solution of the Euler equations which govern approximately the flow field at very high Reynolds numbers around an aircraft. In this inviscid, transonic simulation, the free-stream Mach number is 0.768, and the angle of attack is 1.116° . We use a finite element mesh made of tetrahedral elements. This mesh has 106 064 nodes and 575 986 elements, and was provided to us by Professor Dimitri Mavripilis of Princeton University.

The computation starts with the free-stream values as initial condition, and by using our explicit, local time stepping algorithm, 513 365 equations are solved at each non-linear iteration. In Fig. 12, the top image shows the mesh in the symmetry plane and the Mach number distribution on the aircraft surface. The second image shows the streamlines and surface pressure distribution near the engine. For more details see [15].

6. Concluding remarks

We have reviewed our work on parallel finite element computation of compressible and incompressible flows. These computations were carried out on the Connection Machines CM-5 and CM-200, and

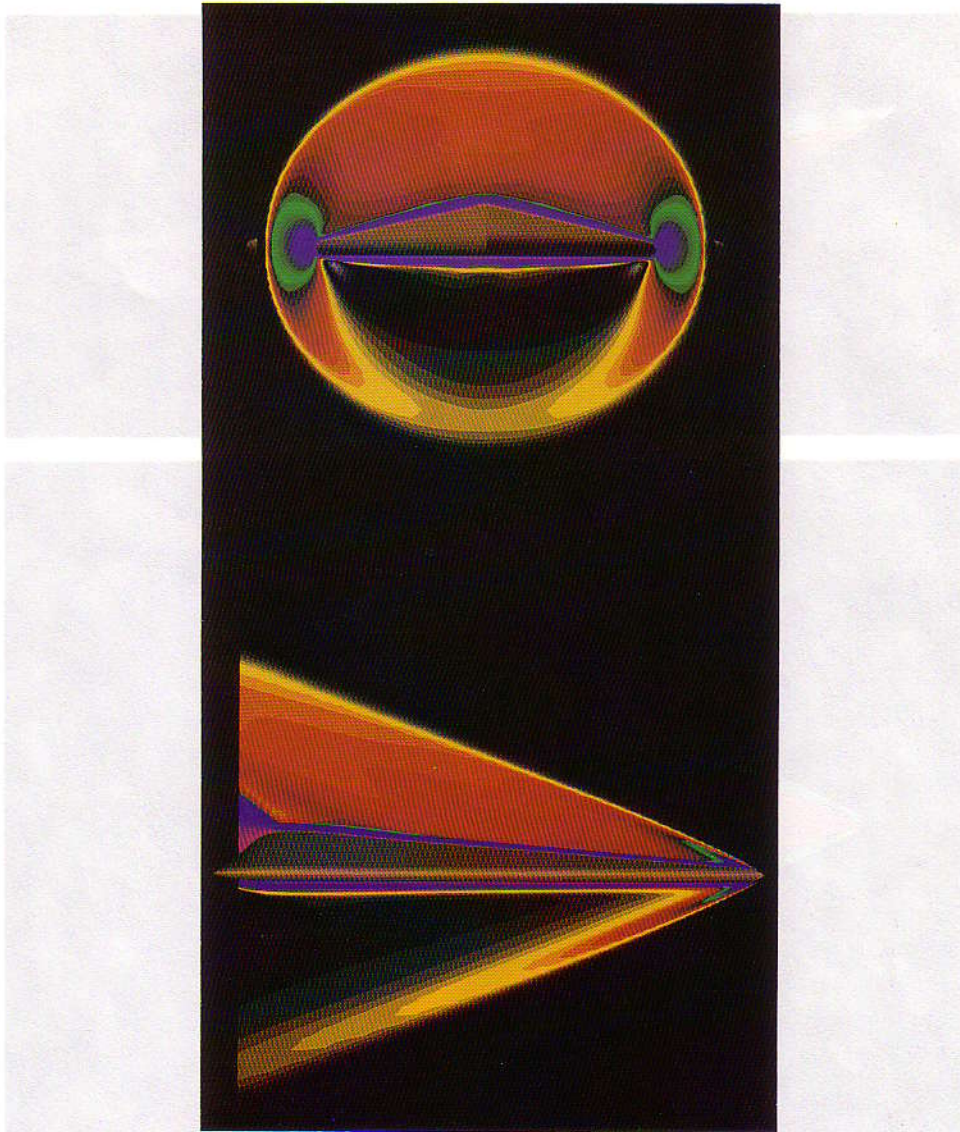


Fig. 10. 3D steady-state, supersonic flow past a delta-wing at Mach 3 and Reynolds number 1.1 million. The images show the side and front views of the delta-wing together with the Mach number distribution around it. Number of non-linear equations solved at every time step is 725 000+. These images appeared on the cover page of the Slide Book of the ARPA High Performance Computing Software PI Meeting, Norfolk, Virginia, 17–18 March 1993.

were based mostly on implicit methods. The parallel implementations are always based on the assumption that the finite mesh is unstructured. We summarize the parallel 3D computation performance on the CM-5 with 512 processing nodes for selected problems in Tables 1 and 2. We note a large disparity between the times required for a single non-linear iteration for these two problems. This is because in the submarine problem, we use a space-time formulation, and a greater number of inner and outer GMRES iterations are needed for convergence in incompressible flows.

Table 1

Flow around a submarine: performance for implicit incompressible flow implementation. Total number of GMRES iterations per non-linear iteration is 200

Computation rate (GigaFLOPS)	7.0
Non-linear iteration cost (s/iteration)	29.3
Non-linear iteration cost (μ s/iteration/node)	206.5

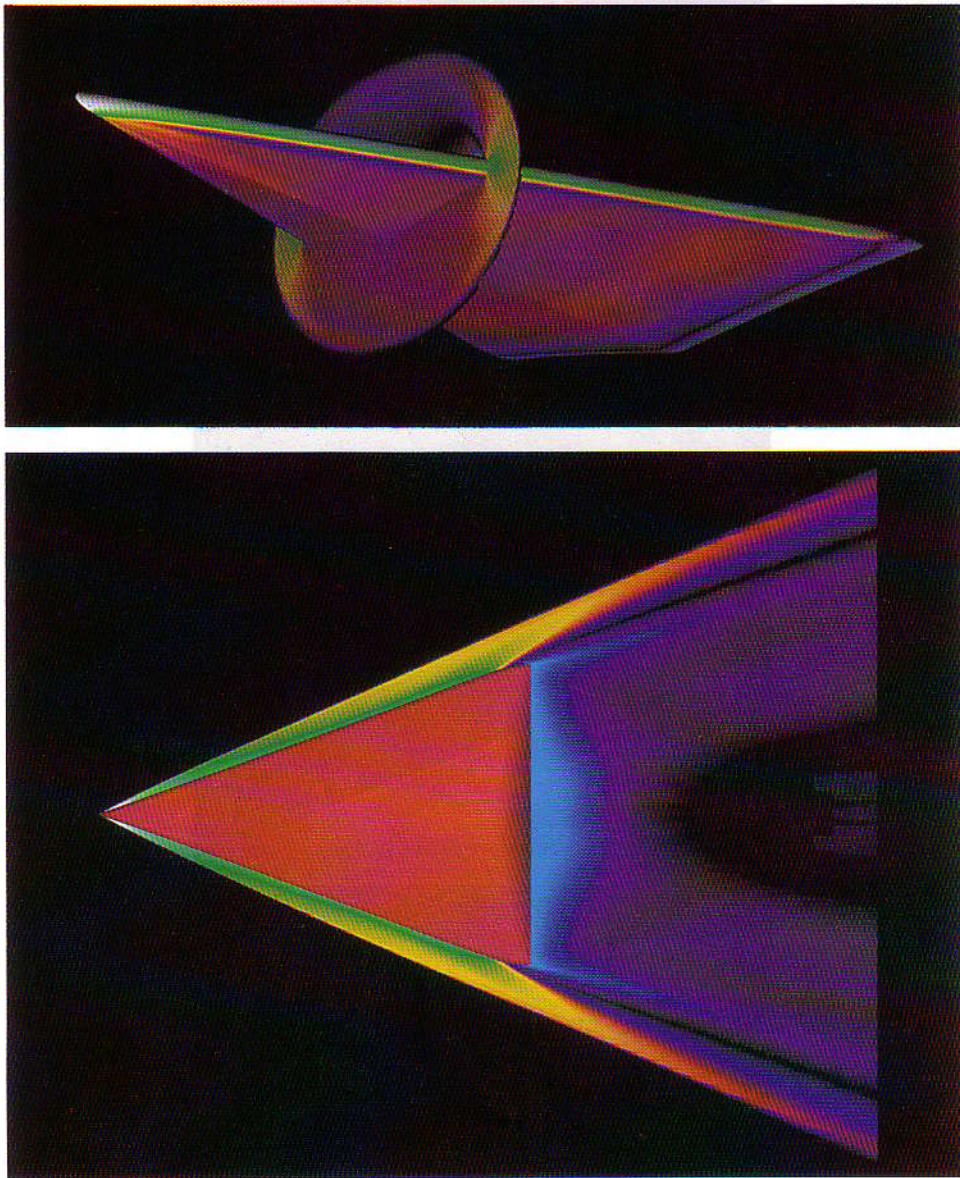


Fig. 11. 3D steady-state, supersonic flow past a delta-wing at Mach 3 and Reynolds number 1.1 million. The top image shows the pressure distribution on the wing surface and at a cross-section. The second image shows the top view of the delta-wing together with the pressure field around it. Number of non-linear equations solved at every time step is 5 000 000+.

We have demonstrated that today we are at a point where we have the capability to solve a large class of practical problems, including those involving moving boundaries and interfaces and those in 3D, using implicit formulations with problem sizes over 5 000 000 equations and computational speeds at 12 GigaFLOPS. We believe this new capability has pushed large-scale finite element computation of flow problems to a new era in numerical simulation.

Table 2

Flow past a delta-wing at Mach 3 and Reynolds number 1.1 million: performance for implicit compressible flow implementation. Total number of GMRES iterations per non-linear iteration is 10.

Computation rate (GigaFLOPS)	9.8
Non-linear iteration cost (s/iteration)	14.9
Non-linear iteration cost (μ s/iteration/node)	14.5

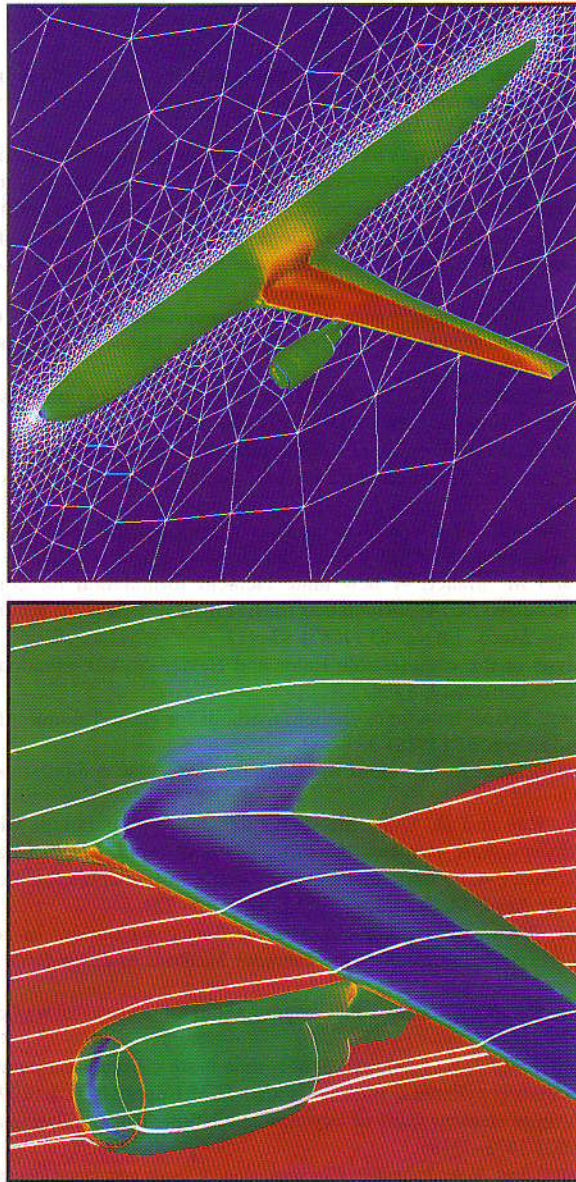


Fig. 12. Steady-state, inviscid, transonic flow past an aircraft at Mach 0.768. The top image shows the mesh in the symmetry plane and the Mach number distribution on the aircraft surface. The second image shows the streamlines and surface pressure distribution near the engine. Number of non-linear equations solved at every time step is 513 000+

Acknowledgment

We thank Dr. Chien Li of NASA-JSC for the surface geometry of the delta-wing, Vinay Kalro for the sphere mesh, and Professor Dimitri Mavriplis of Princeton University for the aircraft mesh. We are also grateful to Bob Haimes of MIT for permission to use of his Visual3 visualization package.

This research was sponsored by NASA-JSC under grant NAG 9-449, by NSF under grants CTS-8796352 and ASC-9211083, by ARPA under NIST contract 60NANB2D1272, and by ARO under grant DAAH04-93-G-0514. Partial support for this work has also come from the ARO contract number DAAL03-89-C-0038 with the AHPCRC at the University of Minnesota.

References

- [1] T.E. Tezduyar, M. Behr and J. Liou, A new strategy for finite element computations involving moving boundaries and interfaces – the deforming-spatial-domain/space–time procedure: I. The concept and the preliminary tests, *Comput. Methods Appl. Mech. Engrg.* 94 (1992) 339–351.
- [2] T.E. Tezduyar, M. Behr, S. Mittal and J. Liou, A new strategy for finite element computations involving moving boundaries and interfaces – the deforming-spatial-domain/space–time procedure: II. Computation of free-surface flows, two-liquid flows, and flows with drifting cylinders, *Comput. Methods Appl. Mech. Engrg.* 94 (1992) 353–371.
- [3] T.E. Tezduyar and T.J.R. Hughes, Finite element formulations for convection dominated flows with particular emphasis on the compressible Euler equations, in: *Proc. AIAA 21st Aerospace Sciences Meeting, AIAA Paper 83-0125*, Reno, Nevada, 1983.
- [4] G.J. Le Beau and T.E. Tezduyar, Finite element computation of compressible flows with the SUPG formulation, in: M.N. Dhaubhadel, M.S. Engelman and J.N. Reddy, eds., *Advances in Finite Element Analysis in Fluid Dynamics, FED – Vol. 123* (ASME, New York, 1991) 21–27.
- [5] S. Aliabadi, S.E. Ray and T.E. Tezduyar, SUPG finite element computation of compressible flows with the entropy and conservation variables formulations, *Comput. Mech.* 11 (1993) 300–312.
- [6] T.J.R. Hughes, L.P. Franca and G.M. Hulbert, A new finite element formulation for computational fluid dynamics: VIII. The Galerkin/least-squares method for advective–diffusive equations, *Comput. Methods Appl. Mech. Engrg.* 73 (1989) 173–189.
- [7] P. Hansbo and A. Szepessy, A velocity–pressure streamline diffusion finite element method for the incompressible Navier–Stokes equations, *Comput. Methods Appl. Mech. Engrg.* 84 (1990) 175–192.
- [8] T.J.R. Hughes, L.P. Franca and M. Mallet, A new finite element formulation for computational fluid dynamics: VI. Convergence analysis of the generalized SUPG formulation for linear time-dependent multi-dimensional advective–diffusive systems, *Comput. Methods Appl. Mech. Engrg.* 63 (1987) 97–112.
- [9] F. Shakib, Finite element analysis of the compressible Euler and Navier–Stokes equations, Ph.D. Thesis, Department of Mechanical Engineering, Stanford University, 1988.
- [10] T.J.R. Hughes and G.M. Hulbert, Space–time finite element methods for elastodynamics: formulations and error estimates, *Comput. Methods Appl. Mech. Engrg.* 66 (1988) 339–363.
- [11] T.E. Tezduyar, Stabilized finite element formulations for incompressible flow computations, *Adv. Appl. Mech.* 28 (1991) 1–44. 1992 →
- [12] T.E. Tezduyar, S. Mittal, S.E. Ray and R. Shih, Incompressible flow computations with stabilized bilinear and linear equal-order-interpolation velocity–pressure elements, *Comput. Methods Appl. Mech. Engrg.* 95 (1992) 221–242.
- [13] S. Aliabadi and T.E. Tezduyar, Space–time finite element computation of compressible flows involving moving boundaries and interfaces, *Comput. Methods Appl. Mech. Engrg.* 107 (1993) 209–224.
- [14] S. Aliabadi and T.E. Tezduyar, Massively parallel compressible flow computations in aerospace applications, *Extended Abstracts of the Second Japan–US Symposium on Finite Element Methods in Large-Scale Computational Fluid Dynamics*, Tokyo, Japan, 1994.
- [15] S. Aliabadi and T.E. Tezduyar, Parallel fluid dynamics computations in aerospace applications, *Int. J. Numer. Methods Fluids*, ~~to appear~~ 21 (1995) 783–805.
- [16] S. Mittal, A. Ratner, D. Hastreiter and T.E. Tezduyar, Space–time finite element computation of incompressible flows with emphasis on flows involving oscillating cylinders, *Internat. Video J. of Engrg. Res.* 1 (1991) 83–96.
- [17] S. Mittal and T.E. Tezduyar, A finite element study of incompressible flows past oscillating cylinders and airfoils, *Internat. J. Numer. Methods Fluids* 15 (1992) 1073–1118.
- [18] T.E. Tezduyar, M. Behr, S. Mittal and A.A. Johnson, Computation of unsteady incompressible flows with the finite element methods – space–time formulations, iterative strategies and massively parallel implementations, in: P. Smolinski, W.K. Liu, G. Hulbert and K. Tamma, eds., *New Methods in Transient Analysis, AMD – Vol. 143* (ASME, New York, 1992) 7–24.
- [19] M. Behr, A. Johnson, J. Kennedy, S. Mittal and T.E. Tezduyar, Computation of incompressible flows with implicit finite element implementations on the Connection Machine, *Comput. Methods Appl. Mech. Engrg.* 108 (1993) 99–118.
- [20] S. Mittal and T.E. Tezduyar, Massively parallel finite element computation of incompressible flows involving fluid-body interactions, *Comput. Methods Appl. Mech. Engrg.* 112 (1994) 253–282.
- [21] S. Mittal and T.E. Tezduyar, Massively parallel finite element simulation of incompressible flows, *Extended Abstracts of the Second Japan–US Symposium on Finite Element Methods in Large-Scale Computational Fluid Dynamics*, Tokyo, Japan, 1994.
- [22] S. Mittal and T.E. Tezduyar, Parallel finite element simulation of 3D incompressible flows-fluid-structure interactions, *Int. J. Numer. Methods Fluids*, ~~to appear~~ 21 (1995) 933–953.
- [23] T. Tezduyar, S. Aliabadi, M. Behr, A. Johnson and S. Mittal, Massively parallel finite element computation of three-dimensional flow problems, in: *Proc. 6th Japan Numerical Fluid Dynamics Symposium*, Tokyo, Japan (1992) 15–24.
- [24] T. Tezduyar, S. Aliabadi, M. Behr, A. Johnson and S. Mittal, Parallel finite-element computation of 3D flows, *IEEE Comput.* 26(10) (1993) 27–36.
- [25] A.A. Johnson and T.E. Tezduyar, Mesh update strategies in parallel finite element computations of flow problems with moving boundaries and interfaces, *Comput. Methods Appl. Mech. Engrg.* 119 (1994) 73.
- [26] D.R. Lynch, Unified approach to simulation on deforming elements with application to phase change problems, *J. Comput. Phys.* 47 (1982) 387–411.

- [27] M. Behr and T.E. Tezduyar, Finite element solution strategies for large-scale flow simulations, *Comp. Methods Appl. Mech. Engrg.* 112 (1994) 3–24.
- [28] J.G. Kennedy, V. Kalro, M. Behr and T.E. Tezduyar, A strategy for implementing implicit finite element methods for incompressible fluids on the CM-5, *Extended Abstracts of the Second Japan–US Symposium on Finite Element Methods in Large-Scale Computational Fluid Dynamics*, Tokyo, Japan, 1994.
- [29] J.G. Kennedy, M. Behr, V. Kalro and T.E. Tezduyar, Implementation of implicit finite element methods for incompressible flows on the CM-5, *Comput. Methods Appl. Mech. Engrg.* 119 (1994) 95.
- [30] Y. Saad and M. Schultz, GMRES: A generalized minimal residual algorithm for solving nonsymmetric linear systems, *SIAM J. Scientific and Statistical Comput.* 7 (1986) 856–869.
- [31] D. Coles, Transition in circular Couette flow, *J. Fluid Mech.* 21 (1965) 385–425.
- [32] Z.C. Feng and P.R. Sethna, Symmetry-breaking bifurcations in resonant surface waves, *J. Fluid Mech.* 199 (1989) 495–518.
- [33] C. Kato and M. Ikegawa, Large eddy simulation of unsteady turbulent wake of a circular cylinder using the finite element method, in: I. Celik, T. Kobayashi, K.N. Ghia and J. Kurokawa, eds., *Advances in Numerical Simulation of Turbulent Flows, FED – Vol. 117* (ASME, New York, 1991) 49–56.
- [34] M.P. Paidoussis and N.T. Issid, Dynamic stability of pipes conveying fluid, *J. Sound and Vibration* 33 (1974) 267–294.
- [35] H. Schlichting, *Boundary-Layer Theory*, 7th edition (McGraw-Hill, New York, 1979).